The Astrophysical Journal, 888:10 (12pp), 2020 January 1 https://doi.org/10.3847/1538-4357/ab557b

Collision and Radiative Parameters for Cr II Lines Observed in Stellar and Nebular Spectra

S. S. Tayal[1] and O. Zatsarinny[2]
[1] Department of Physics, Clark Atlanta University, Atlanta, GA 30314, USA; stayal@cau.edu
[2] Department of Physics and Astronomy, Drake University, Des Moines, IA, 50311, USA
Received 2019 August 23; revised 2019 November 4; accepted 2019 November 6; published 2019 December 27

Abstract

Electron excitation collision strengths (Ω) and transition probabilities (*A*-values) for the iron-peak element Cr II lines are of high importance for the stellar and nebular abundance studies. Collision and radiative parameters are presented for all possible inelastic transitions between the Cr II 512 fine-structure levels covering infrared to extreme ultraviolet lines. These parameters should allow a detailed modeling and analysis of the available measured stellar and nebular spectra from different astrophysical objects. Accurate target wave functions have been generated using the multiconfiguration Hartree–Fock method together with term-dependent one-electron orbitals and well-chosen configuration expansions. The wave functions are then used in the calculations of transition probabilities and collision rates. The *B*-spline Breit–Pauli *R*-matrix method has been employed for the calculation of electron excitation collision strengths. The semiempirical fine-tuning procedure has been applied to the energies of the local supercluster (LS) terms prior to transformation of the Hamiltonian matrices to intermediate coupling. The Hamiltonian matrices for the calculation of collision rates also include spin–orbit interaction. The 512 fine-structure levels of the Cr II $3d^5$, $3d^44s$, $3d^34s^2$, $3d^44p$, and $3d^34s4p$ configurations have been considered in our work. The thermally averaged collision strengths have been determined using a Maxwellian distribution for a wide range of temperatures from 10^2 to 10^5 K. The accuracy of our results has been estimated by comparison with other calculated collision rates and available measured radiative rates.

Unified Astronomy Thesaurus concepts: Atomic spectroscopy (2099); Laboratory astrophysics (2004)

Supporting material: machine-readable tables

1. Introduction

The radiative and collision rates of Cr II are of significant importance for the analysis and interpretation of stellar and nebular spectra. The singly ionized Cr ion is predominant in the astrophysical objects with effective temperature in the range 5000–10,000 K. There are several abundance studies that have emphasized the need for accurate atomic parameters for Cr II (Babel & Lanz 1992; Rice & Wehlau 1994; Dimitrijevic et al. 2007; Wallace & Hinkle 2009; Lawler et al. 2017). Discrepancies exist in the abundance pattern of iron-peak elements with metallicity in metal-poor stars (Sneden et al. 2003; Barklem et al. 2005). A large number of emission lines of iron-peak elements including Cr II have been detected in the spectra of strontium filament of η Carinae, which is a hot and luminous central star with cool circumstellar nebula. The Cr II lines are especially strong in the spectra of several chemically peculiar stars (Lopez-Garcia et al. 2001). Many models used in these studies are still hindered by the lack of reliable oscillator strengths and rate constants for inelastic collisions.

There are several experimental studies available for the oscillator strengths and transition probabilities of Cr II lines; however, they cover a relatively small number of transitions needed in the abundance studies. First, an extended set of wavelengths and oscillator strengths from the 25 lowest odd parity energy levels has been reported by Nilsson et al. (2006). They presented oscillator strengths for 119 lines derived from line intensity ratios determined from Fourier transform spectra and combined with lifetimes from time-resolved laser-induced fluorescence measurements. Later, Gurell et al. (2010) presented laboratory measurements of transition probabilities for 145 Cr II lines and radiative lifetimes for 14 Cr II levels, yielding experimental transition probabilities for strong lines in stellar spectra. Recently, Lawler et al. (2017) reported new radiative lifetime measurements for eight levels and branching fraction measurements for 183 lines of Cr II. All 8 lifetimes and 102 of the branching fractions overlap with Nilsson et al. (2006), allowing a more detailed discussion of the uncertainties. The lifetimes for low-lying metastable levels of Cr II received much less attention. We are aware of only one measurement of Backstrom et al. (2012) who reported lifetimes for two metastable $3d^44s$ $^4D_{5/2}$ and $^4D_{7/2}$ levels.

Most extended theoretical studies of oscillator strengths were carried out in the semiempirical approximations. These studies include the calculations by Kurucz (1988) using the Cowan code, by Raassen & Uylings (1998) using the orthogonal operator method, and most recently by Bouazza et al. (2019) using a pseudo-relativistic Hartree–Fock model with empirically adjusted radial integral values. Wasson et al. (2011) reported oscillator strength calculations based on the structure code CIV3 (Hibbert 1975). It is the largest calculation so far for the optically allowed transitions between the 280 Cr II levels; however, their configuration expansions were restricted by the feasibility requirement in the following scattering calculations. Clearly further work on radiative transition rates is required.

Until recently there was an apparent lack of the collision data available in the literature for the electron-impact excitation of Cr II. Bautista et al. (2009) carried out the first ab initio calculations of radiative transition rates and electron-impact excitation rate coefficients, which were applied in their study of chemical abundances of the strontium filament found in the ejecta of η Carinae. They used the local supercluster (LS) *R*-matrix plus algebraic transformation method and the collision strengths for transitions between the lowest 162 fine-structure levels belonging to the $3d^5$, $3d^44s$, and $3d^44p$ configurations were evaluated but not published. More elaborated and extended calculations were reported by Wasson et al. (2010, 2011). They used the parallel suite of *R*-Matrix packages, RMATRIX II (Burke et al. 1994) plus FINE procedure, which transforms the *R*-Matrix in LS-coupling at energy *E* into an *R*-matrix in pair coupling. A total of 108 LS states giving rise to 280 fine-structure levels from the basis configurations $3d^5$, $3d^44s$, and $3d^44p$ were included in the wave function representation of the target belonging to all doublet, quartet, and sextet terms. They first reported the data for low-lying forbidden lines among the lowest 74 fine-structure levels of Cr II (Wasson et al. 2010). Later they considered the dipole-allowed lines for transitions from the $3d^5$ and $3d^44s$ even-parity configuration states to the $3d^44p$ odd parity configuration states (Wasson et al. 2011). The accuracy of the effective collision strengths for the important low-lying forbidden lines was estimated to be within 15%. For the higher lying lines, larger discrepancies would be expected due to the omission of higher lying $3d^34s4p$ states in the close-coupling (CC) expansion. Comparison with the work of Bautista et al. (2009) for the optically allowed transitions revealed some significant discrepancies.

Conclusive assessment of the accuracy of effective collision strengths for Cr II still remains difficult, especially since we have only two calculations for comparison, which were performed by employing the Belfast *R*-matrix codes. The reliable theoretical study of low-energy electron collision requires both an accurate target description and a sufficient number of target states in the CC expansion to achieve convergence for the transitions of interest. For Cr II ion, as for other iron-peak elements, the convergence is very difficult to achieve due to their complicated structures caused by the presence of the open 3*d*-shell. A very large number of energy levels needs to be considered in the CC expansions for a reasonable convergence of results. It is a challenging task to obtain accurate description of target states for the open *d*-shell atomic systems with the standard configuration-interaction (CI) procedures. The individual orbitals in the 3*d*-shell with different occupation are term dependent. In the case of orthogonal one-electron orbitals, as noted by Wasson et al. (2010), accurate representations of both the Cr II target and the collision wave functions require a careful balance between the size and accuracy.

The *B*-spline *R*-matrix (BSR) method with the term-dependent nonorthogonal orbitals (Zatsarinny 2006) offers several advantages for electron collision calculations of the complex iron-peak elements. The use of term-dependent sets of one-electron orbitals provides accurate target description as demonstrated in our recent calculations for electron-impact excitation of Fe II (Tayal & Zatsarinny 2018). Our aim here is to carry out extensive calculations for the electron collision with Cr II to provide an independent test for the existing data sets and to obtain a more realistic estimate of the accuracy of collision parameters. We compute collision and radiative rates for fine-structure transitions between the Cr II 512 levels arising from the primary $3d^44s$, $3d^5$, $3d^44p$, $3d^34s^2$, and $3d^34s4p$ configurations. This corresponds to a substantially large 3492 coupled channels problem. The inclusion of the $3d^34s^2$ and $3d^34s4p$ configurations allows us to explore the influence of strong 3*d*–4*p* and 3*d*–4*s* excitations, not considered before, and check the convergence of the CC expansions. We employ very accurate target wave functions in our collision calculations. Beside the use of flexible term-dependent orbitals, we also carefully checked the correlation corrections related to all single and double excitations from the main configurations. The CC expansions include one-body spin–orbit interaction directly through the Breit–Pauli Hamiltonian. A fine-tuning procedure was used to adjust the target LS energies to the experimental values for accurate representation of the spin–orbit mixing of different terms. This improves the accuracy of the term-mixing coefficients in the target wave functions which in turn enhances the accuracy of weaker forbidden transitions.

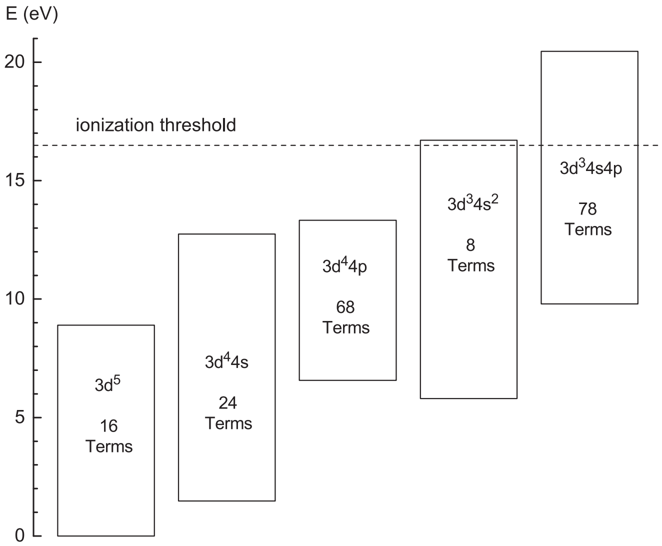

Figure 1. Lower terms of the Cr II spectrum.

2. Computational Methods

2.1. Wave Function Calculations

The lower terms of the Cr II spectrum included in the present calculations are shown in Figure 1. The half-open 3*d* shell results in a large number of LS energy levels. The levels from the lowest $3d^5$, $3d^44s$, $3d^44p$, and $3d^34s^2$ configurations overlap with each other and thus may have strong configuration interaction. The electron correlation effects between the valence 3*d*, 4*s*, and 4*p* electrons may also be significant. The accurate representation of electron correlation effects in atomic systems with open 3d-shell requires inclusion of one and two valence electron excitations to the excited orbitals in the configuration-interaction (CI) expansions leading to very large expansions. The convergence of the CI expansions becomes slower due to the term-dependence of the valence orbitals. The use of nonorthogonal one-electron orbitals in the CI expansions of the target states is an important feature of the BSR scattering code. In the present calculations for the Cr II target states, we accounted for all important correlation corrections with reasonable size of final multiconfiguration target expansions which could be managed in the scattering calculations with $(N + 1)$-electrons.

The MCHF code of Froese Fischer et al. (2007) together with the CI code with nonorthogonal orbitals (Zatsarinny & Froese Fisher 2000, 2009) were employed to determine the Cr II target wave functions. The core 1*s*, 2*s*, 2*p*, 3*s*, and 3*p* orbitals were determined using the Hartree–Fock method on the ground $3d^5\ ^6S$ state and the same set of core orbitals was used for all states. The term-dependence of the valence $3d$, $4s$, and $4p$ orbitals was accounted for by optimization on chosen terms of each principal configuration in the term-average approximation. The average radius of the $3d$ orbital is 1.36, 1.21, and 1.10 au for the $3d^5$, $3d^44s$, and $3d^34s^2$ configurations, respectively, indicating the significance of term-dependence of valence orbitals. The corrections in the configuration energies due to the use of term-dependent orbitals were found to be around 2.7 eV. In addition to valence spectroscopic orbitals, several sets of nonorthogonal correlation $4l$ and $5l$ ($l = 0$–3) orbitals were determined for each primary configuration. Each set of correlation orbitals has been generated using the MCHF procedure for one specific term and then the same set has been used for all terms of a given configuration. We attempted to keep the target expansions to a reasonable size by including the most important correlation effects. We first considered the detailed target expansions containing all one- and two-electron excitations and then used a cutoff parameter to drop the insignificant correlation configurations from the target expansions.

Table 1 lists the primary configurations along with important correlation configurations and their average mixing coefficients in the target CI expansions. The correlated orbitals have mean radii close to the outer valence $3d$, $4s$, and $4p$ orbitals in the primary configurations. The correlation patterns for different primary configurations differ from each other significantly. As a general trend, the $3d^2$–$4d^2$ substitution along with other two-electron excitations from the 3d shell, $3d^2$–$4p^2$ and $3d^2$–$4f^2$, make the major correlation contributions. These two-electron excitations exhibit the $3d$ inner-shell correlation, and should be different for the $3d^5$, $3d^44s$, and $3d^34s^2$ primary configurations as the number of $3d$ electrons is different. Wasson et al. (2010) included $3d^34d^2$ configurations, but none of the $3d^24d^24s$ configurations that provide dominant corrections for the $3d^44s$ states. The expansions of Wasson et al. (2010) and Bautista et al. (2009) also included the configurations with one and two-electron excitations of the inner $3s$ and $3p$ shells. These two-electron excitations should be approximately the same for all target states and should not effect the relative position of target states.

The electron correlation effects due to $3d$–$4f$ excitations are also significant as can be noted from the Table 1. No such configurations were included in the previous calculations. The large correlation contributions of $4f$ correlated orbitals are due to the fact that the $4f$ correlated orbital and the $3d$ valence orbital have similar radius. For the $3d^44s$ states, the $3d$–$4s$ intershell correlation reflects in the large contributions of the $3d^34p^2$ and $3d^34p4f$ configurations corresponding to the dipole interaction $3d4s$–$4p^2$ and $3d4s$–$4p4f$, respectively. The $3d$–$4p$ intershell correlation in the $3d^44p$ states is important for the same reason. The large contribution of the $3d^34p5s$ correlation configuration in the $3d^44p$ states is due to the $3d4p$–$4p5s$ dipole interaction. The $3d^34s^2$ states mix strongly with the $3d^34p^2$ configuration. The correlation effects between two valence electrons are exhibited by the large mixing of the $3d^34s5p$ and $3d^34p4d$ correlation configurations with the $3d^34s4p$ states.

All configurations with mixing coefficients smaller than ~0.02 were removed from the target CI expansions. The cutoff parameter provided the CI expansions of size from 200 to 400 for each LS target state. As a next step we adjusted the theoretical LS energies to the weighted average of experimental values (Kramida et al. 2015). The convergence was quickest for the sextet terms and slowest for the doublet terms. The cutoff parameters were varied from 0.015 to 0.030 for the different terms because of their different convergence patterns. An agreement of better than 0.1 eV with observed LS energies was achieved for all considered states in our calculation.

Table 1
Main Correlation Contributions

Primary Configuration	Correlation Configuration	Mixing Coefficient
$3d^5$	$3d^34d^2$	0.0609
	$3d^44d$	0.0517
	$3d^34p^2$	0.0366
	$3d^34f^2$	0.0293
$3d^44s$	$3d^24d^24s$	0.0477
	$3d^34p^2$	0.0374
	$3d^24f^24s$	0.0277
	$3d^45s$	0.0274
	$3d^34p4f$	0.0260
$3d^34s^2$	$3d^34p^2$	0.2105
	$3d^34s4d$	0.0508
	$3d4s^24d^2$	0.0392
	$3d^34s5s$	0.0391
	$3d^24s4p4f$	0.0380
	$3d^24s4f^2$	0.0337
	$3d^24s4p^2$	0.0257
	$3d^35s^2$	0.0250
	$3d^34d^2$	0.0215
$3d^44p$	$3d^34p5s$	0.0710
	$3d^45p$	0.0438
	$3d^24p4d^2$	0.0418
	$3d^34p4d$	0.0397
	$3d^24p5s^2$	0.0314
	$3d^34f5s$	0.0305
	$3d^24p5f^2$	0.0294
	$3d^34d4f$	0.0244
	$3d^35s5p$	0.0233
	$3d^34d5p$	0.0218
$3d^34s4p$	$3d^34p4d$	0.1013
	$3d^34s5p$	0.0889
	$3d4d^24s4p$	0.0414
	$3d^24p^24f$	0.0316
	$3d4f^24s4p$	0.0295
	$3d^35s5p$	0.0277
	$3d^34d5p$	0.0247
	$3d^34s4f$	0.0227
	$3d^24s4p4d$	0.0204

The Breit–Pauli Hamiltonian matrices are diagonalized to determine J-dependent target states. The target expansions for total angular momentum J and parity π are written as a sum over different LS values that couple to give J as follows

$$\Psi^{\beta J\pi} = \sum_{\alpha \mathrm{LS}} C(\beta J\pi;\, \alpha\mathrm{LS}\pi)\,\Phi^{\alpha \mathrm{LS}\pi}. \tag{1}$$

We included one-body mass, Darwin, and spin–orbit Breit–Pauli operators in our calculations and we did not use any cutoff factor at this stage. The final target expansions contained an average of 1000 configurations. The multiconfigurational expansions from the LS calculations are represented by the functions $\Phi^{\alpha \mathrm{LS}\pi}$, and the coefficients $C(\beta J\pi;\ \alpha \mathrm{LS}\pi)$ provide the spin–orbit mixing of different LS terms. The representation of term mixing is very important and depends both on the spin–orbit interaction as well as the closeness of the LS states. Further semiempirical corrections to the energies of the $\Phi^{\alpha \mathrm{LS}\pi}$ functions were made to improve the term mixing by adjusting theoretical values closely to the observed values. These adjustments are less than 0.1 eV and are made to improve the agreement with the observed Cr II spectrum. The fine-tuning of calculated target energies to experimental values is a standard procedure that has been regularly used to improve the structure calculations (Hibbert 1996).

2.2. Collision Calculations

The scattering calculations have been performed by employing an extended version of the parallelized BSR code (Zatsarinny 2006) to solve CC equations. The calculations in the present work were carried out in a manner similar to our recent calculations of electron scattering on Fe II (Tayal & Zatsarinny 2018). We only summarize the specific features for the present case below. First we have performed the LS calculations for transitions between LS terms, and then the Hamiltonian matrices in the inner region were transformed to the intermediate coupling to obtain collision strengths between fine-structure levels. This procedure is equivalent to the direct Breit–Pauli *R*-matrix calculations without the need of repeating calculations of matrix elements for nonrelativistic Hamiltonian for the different *J*-values. The nonrelativistic Hamiltonian matrices were obtained for the 194 LS states of the $3d^44s$, $3d^34s^2$, $3d^5$, $3d^44p$, and $3d^34s4p$ configurations. These calculations involved up to 591 different scattering channels. The calculations were carried out for 408 partial waves up to $L = 50$ and total spin $S = 0$–3. The inner region was chosen to have a radius of 20 a_0. We used 86 *B*-splines of order 8 to represent the continuum orbitals giving rise to the Hamiltonian matrices with dimensions up to 50,000. A large number of different two-electron matrix elements are involved in the construction of the Hamiltonian matrices both due to the large configuration expansions and the large number of overlap factors arising from the nonorthogonal orbitals.

In the second step, we determined the Breit–Pauli matrices using the BSR_RECOUP program of the BSR complex as discussed in our recent calculations for Fe II (Tayal & Zatsarinny 2018). The spin–orbit interaction of the scattering electron was included in the Hamiltonian matrices. The 512 fine-structure levels of the Cr II $3d^44s$, $3d^34s^2$, $3d^5$, $3d^44p$, and $3d^34s4p$ configurations were considered in the scattering model. The Breit–Pauli *R*-matrix calculations were carried out for 50 lower partial waves of both even and odd parities and for 2*J* up to 48. The parallel version of the STGF program (Ballance & Griffin 2004) has been used to calculate the asymptotic solutions in the outer region and subsequently the collision strengths as a function of electron energies. It is a powerful program that is capable of treating large expansions in the external region; however, in the present calculations we carried out our calculations for each partial wave separately and then summed the results to determine total collision strengths. This allows us to avoid extremely large H.DAT files due to large dimensions of the Hamiltonian matrices. We used a fine energy grid of 10^{-4} Ry to include significant resonances below the highest excitation threshold. A coarse electron energy grid of 10^{-2} Ry was used in the nonresonant energy region to calculate collision strengths up to 10 Ry. The collision strengths were calculated at 12,000 electron energies. The asymptotic energy dependence of the collision strengths Ω for the various dipole-allowed and forbidden transitions were used to extrapolate the results to higher energies. A top-up procedure based on the Coulomb–Bethe method or on geometric series approximation was employed to estimate higher partial wave contributions (Burgess 1974).

The effective collision strengths $\Upsilon(T_e)$ have been calculated by convoluting the collision strength Ω with a Maxwellian distribution for electron temperature T_e, i.e.,

$$\Upsilon_{i-j}(T_e) = \int_{E_{\mathrm{th}}}^{\infty} dE\ \Omega_{i-j}(E)\exp\left(-\frac{E - E_{\mathrm{th}}}{kT_e}\right). \tag{2}$$

Here E_{th} is the *i–j* transition energy and *k* is the Boltzmann constant. We calculated Υ for temperatures from 10^2 to 10^5 K.

3. Results and Discussion

3.1. Radiative Parameters

We considered 512 fine-structure levels in the CC expansion and their excitation energies and lifetimes are given in machine-readable format. The present excitation energies for the lowest 100 levels of Cr II are given in Table 2 where the calculated values have been compared with experimental energies from the NIST compilation (Kramida et al. 2015). We have ordered the fine-structure levels using the order of their LS terms. The positions of energy levels are given by indices in the first column of the table. These indices are used in the following discussion to denote different transitions. There is very good agreement between the present excitation energies and experimental values. For the majority of the energy levels the difference is in the range of a few meV. It means that our results show better agreement than the previous calculations for Cr II. It is made possible by the semiempirical fine-tuning and other procedures used in our calculations. These procedures are designed to retain all strong CI effects and to represent mixing of the spin–orbit terms.

We have presented line strengths, oscillator strengths, and decay probabilities both for the dipole-allowed (E1) and dipole-forbidden (M1 and E2) transitions in Table 3. There are many even-parity metastable levels in the Cr II spectrum that can decay to lower levels via forbidden electric quadrupole (E2) and magnetic dipole (M1) transitions only. Such parity forbidden radiative transitions are observed in spectra of low density astrophysical plasmas and can be used as probes of the physical conditions. There are a limited number of experimental lifetimes available for the metastable levels in Cr II. The radiative lifetimes of the metastable energy levels $3d^44s\ c^4D_{5/2}$ and $3d^44s\ c^4D_{7/2}$ of Cr II have been measured by Backstrom et al. (2012). They present the lifetimes of these levels to be $\tau_{5/2} = 1.28(16)$ s and $\tau_{7/2} = 1.37(7)$ s, respectively. These values are in close agreement with the present results of $\tau_{5/2} = 1.23$ s and $\tau_{7/2} = 1.30$ s.

The electric-dipole transitions in Cr II received much more attention from experiment. First an extensive set of *f*-values for Cr II was presented by Nilsson et al. (2006). All upper levels included in their analysis belong to the $3d^4(^5D)4p$ configuration with the same parent term ^5D, giving a total of 25 odd parity levels in the energy range between 47,000 and 55,000 cm^{-1}. The

Table 2
Excitation Energies (in eV) and Lifetimes (in second) of the Cr II Fine-structure Levels

Index	Configuration	Term	J	Present	NIST	τ(s)	Index	Configuration	Term	J	Present	NIST	τ(s)
1	$3d^5$	$a\ ^6S$	5/2	0.0000	0.0000		51	$3d^4(^3F)4s$	$b\ ^2F$	5/2	4.4093	4.4100	1.34E+01
2	$3d^4(^5D)4s$	$a\ ^6D$	1/2	1.4782	1.4830	1.39E+01	52			7/2	4.4151	4.4147	8.52E+00
3			3/2	1.4881	1.4918	1.35E+01	53	$3d^5$	$b\ ^2H$	9/2	4.4169	4.4151	1.76E+01
4			5/2	1.5044	1.5061	1.27E+01	54			11/2	4.4294	4.4271	9.09E+00
5			7/2	1.5266	1.5254	1.18E+01	55	$3d^4(^3G)4s$	$a\ ^2G$	7/2	4.4736	4.4760	3.92E+01
6			9/2	1.5542	1.5493	1.08E+01	56			9/2	4.5018	4.4972	3.42E+01
7	$3d^4(^5D)4s$	$a\ ^4D$	1/2	2.4168	2.4211	5.20E+02	57	$3d^4(^3D)4s$	$c\ ^4D$	7/2	4.7463	4.7448	1.43E+00
8			3/2	2.4313	2.4339	5.32E+02	58			5/2	4.7517	4.7504	1.48E+00
9			5/2	2.4547	2.4546	4.68E+02	59			3/2	4.7569	4.7563	1.47E+00
10			7/2	2.4866	2.4826	4.26E+02	60			1/2	4.7604	4.7605	1.44E+00
11	$3d^5$	$a\ ^4G$	5/2	2.5408	2.5431	2.91E+05	61	$3d^4(^3G)4s$	$b\ ^2G$	7/2	4.7764	4.7745	1.50E+01
14			11/2	2.5451	2.5431	1.75E+05	62			9/2	4.7800	4.7812	1.59E+01
12			7/2	2.5427	2.5438	1.52E+05	63	$3d^4(^1G)4s$	$c\ ^2G$	7/2	4.9247	4.9201	9.68E+00
13			9/2	2.5443	2.5440	1.98E+05	65			9/2	4.9341	4.9375	2.03E+01
16	$3d^5$	$a\ ^4P$	5/2	2.7060	2.7056	8.71E+00	64	$3d^5$	$c\ ^2F$	5/2	4.9278	4.9273	7.15E+00
17			1/2	2.7061	2.7058	5.67E+00	66			7/2	4.9442	4.9441	1.14E+01
15			3/2	2.7059	2.7058	3.11E+02	67	$3d^4(^1I)4s$	$b\ ^2I$	13/2	4.9856	4.9844	1.01E+01
19	$3d^5$	$b\ ^4D$	7/2	3.1048	3.1037	4.83E+01	68			11/2	4.9863	4.9876	1.12E+01
18			1/2	3.1028	3.1039	9.41E+01	69	$3d^4(^1S)4s$	$a\ ^2S$	1/2	5.0112	5.0108	4.17E+00
20			3/2	3.1048	3.1049	6.74E+01	70	$3d^4(^3D)4s$	$b\ ^2D$	5/2	5.3143	5.3186	5.93E+00
21			5/2	3.1064	3.1054	1.04E+02	71			3/2	5.3334	5.3296	7.09E+00
22	$3d^4(^3P)4s$	$b\ ^4P$	1/2	3.7088	3.7135	4.00E+00	72	$3d^5$	$b\ ^2S$	1/2	5.4930	5.4933	4.97E+00
27			3/2	3.7560	3.7576	2.81E+01	73	$3d^4(^1D)4s$	$c\ ^2D$	3/2	5.6600	5.6622	2.74E+00
30			5/2	3.8313	3.8267	1.96E+03	74			5/2	5.6725	5.6698	2.74E+00
24	$3d^5$	$a\ ^2I$	11/2	3.7358	3.7372	1.18E+04	75	$3d^4(^5D)4p$	$z\ ^6F^o$	1/2	5.8042	5.8053	3.90E-09
25			13/2	3.7391	3.7381	2.70E+01	76			3/2	5.8145	5.8155	3.89E-09
23	$3d^4(^3H)4s$	$a\ ^4H$	7/2	3.7346	3.7389	4.41E+00	77			5/2	5.8315	5.8322	3.88E-09
26			9/2	3.7446	3.7466	2.58E+01	78			7/2	5.8550	5.8554	3.85E-09
28			11/2	3.7573	3.7565	2.42E+01	81			9/2	5.8847	5.8848	3.10E+00
29			13/2	3.7725	3.7681	6.02E+00	82			11/2	5.9206	5.9204	2.85E+00
31	$3d^4(^3F)4s$	$a\ ^4F$	3/2	3.8528	3.8537	1.35E+01	80	$3d^5$	$d\ ^2D$	5/2	5.8749	5.8711	3.82E-09
32			5/2	3.8574	3.8580	8.76E+00	79			3/2	5.8697	5.8734	3.79E-09
33			7/2	3.8648	3.8644	6.54E+00	83	$3d^4(^5D)4p$	$z\ ^6P^o$	3/2	5.9953	6.0007	2.14E-09
34			9/2	3.8730	3.8707	5.35E+00	84			5/2	6.0110	6.0121	2.13E-09
35	$3d^5$	$a\ ^2D$	5/2	3.8850	3.8870	8.43E+00	85			7/2	6.0343	6.0296	2.12E-09
36			3/2	3.9070	3.9093	1.56E+01	86	$3d^4(^5D)4p$	$z\ ^4P^o$	1/2	6.0458	6.0441	4.70E-09
37	$3d^5$	$a\ ^2F$	7/2	4.0220	4.0115	1.03E+01	87			3/2	6.0768	6.0759	4.39E-09
38			5/2	4.0520	4.0423	5.95E+00	92			5/2	6.1602	6.1627	3.87E-09
39	$3d^5$	$b\ ^4F$	7/2	4.0715	4.0712	3.37E+00	88	$3d^4(^5D)4p$	$z\ ^6D^o$	5/2	6.1200	6.1188	3.64E-09
40			3/2	4.0720	4.0722	3.31E+00	89			1/2	6.1295	6.1363	3.75E-09
41			9/2	4.0743	4.0734	3.27E+00	90			3/2	6.1397	6.1452	3.38E-09
42			5/2	4.0781	4.0734	3.72E+00	91			7/2	6.1568	6.1553	4.20E-09
43	$3d^4(^3G)4s$	$b\ ^4G$	5/2	4.1392	4.1433	8.64E+00	93			9/2	6.1838	6.1791	3.38E-09
44			7/2	4.1550	4.1560	8.47E+00	94	$3d^4(^1F)4s$	$d\ ^2F$	7/2	6.2812	6.2819	1.79E+00
45			9/2	4.1702	4.1682	8.31E+00	95			5/2	6.2846	6.2844	1.95E+00
46			11/2	4.1818	4.1775	8.09E+00	96	$3d^4(^5D)4p$	$z\ ^4F^o$	3/2	6.3906	6.3956	4.14E-09
47	$3d^4(^3H)4s$	$a\ ^2H$	9/2	4.2890	4.2936	9.57E+01	97			5/2	6.4036	6.4061	4.14E-09
49			11/2	4.3195	4.3162	4.87E+00	98			7/2	6.4219	6.4209	4.14E-09
48	$3d^4(^3P)4s$	$a\ ^2P$	1/2	4.2935	4.2972	5.09E+01	99			9/2	6.4457	6.4400	4.13E-09
50			3/2	4.3880	4.3835	6.80E+00	100	$3d^5$	$d\ ^2G$	7/2	6.4837	6.4841	3.22E-01

(This table is available in its entirety in machine-readable form.)

absolute oscillator strengths were obtained from the emission branching fraction measurements with their normalization to the radiative lifetime measurements from laser-induced fluorescence (Schade et al. 1990). Recently, new measurements of emission branching fraction and radiative lifetimes in Cr II are reported by Lawler et al. (2017). These data can be used to check our target wave functions and estimate the accuracy of our radiative data presented in Table 3.

We have presented a comparison of our calculated transition probabilities for selected E1 transitions with measurements in Table 4 and in Figure 2. The agreement between the present A-values and the experimental results is very satisfactory, with

Table 3
Line Strengths (S), Oscillator Strengths (f), and Transition Probabilities (A) for E1, E2, and M1 Transitions in Cr II

i	k	Type	λ(Å)	S	f_{ik}	A_{ki}(s^{-1})
1	2	E2	8387.26	5.32E+00	2.52E-10	7.18E-02
1	3	E2	8331.44	1.06E+01	5.15E-10	7.42E-02
1	3	M1	8331.44	4.86E-08	3.93E-15	5.66E-07
1	4	E2	8241.32	1.60E+01	7.98E-10	7.83E-02
1	4	E2	8241.32	1.60E+01	7.98E-10	7.83E-02
1	4	M1	8241.32	3.80E-08	3.11E-15	3.05E-07
1	4	M1	8241.32	3.80E-08	3.11E-15	3.05E-07
1	5	E2	8121.60	2.13E+01	1.11E-09	8.43E-02
1	5	M1	8121.60	4.93E-09	4.09E-16	3.11E-08
1	6	E2	7977.00	2.66E+01	1.47E-09	9.22E-02
1	83	E1	2068.04	2.95E+00	7.23E-02	1.69E+08
1	84	E1	2062.62	4.45E+00	1.09E-01	1.71E+08
1	85	E1	2054.67	6.00E+00	1.48E-01	1.75E+08
1	87	E1	2040.27	4.26E-02	1.06E-03	2.54E+06
1	88	E1	2025.87	2.91E-02	7.28E-04	1.18E+06
1	90	E1	2019.39	7.37E-03	1.85E-04	4.53E+05
1	91	E1	2013.79	5.67E-06	1.42E-07	1.76E+02
1	92	E1	2012.66	2.84E-02	7.15E-04	1.18E+06

(This table is available in its entirety in machine-readable form.)

an overall dispersion of 8.3% with the results of Nilsson et al. (2006) and 10.1% with A-values of Lawler et al. (2017). As a general trend, the calculated A-values exceed the experimental values, resulting in calculated level lifetimes lower than the measured values by 10%–20%. The upper levels for transitions are grouped in six ^6F, ^6D, ^6P, ^4F, ^4D, and ^4P terms and the comparison includes both the spin-allowed and spin-forbidden transitions between the sextet and quartet terms. The calculated transition probabilities for the weak spin-forbidden transitions and for the strong spin-allowed transitions show similar agreement with experiment. It indicates that the term mixing due to spin–orbit interaction is correctly represented in our target wave functions. Our target states produce accurately the strong E1 as well as weak M1 and E2 transitions in Cr II indicating the accuracy of our target wave function expansions.

3.2. Collision Parameters

The collision strengths for the forbidden fine-structure $3d^5\ ^6S_{1/2}$–$3d^44s\ ^6D_{1/2}$ (1–2) and $3d^44s\ ^6D_{1/2}$–$3d^44s\ ^4D_{3/2}$ (2–8) transitions have been displayed as a function of incident electron energy (in Ry) in Figure 3. The same transitions were also discussed by Wasson et al. (2011). The collision strengths exhibit rich resonance structure in the low-energy region up to 0.5 Ry. The resonance structure substantially exceeds the nonresonant collision strength and provides dominant contribution to the thermally averaged collision strengths at lower temperatures. It is generally true for the forbidden transitions in electron–ion scattering. The resonance structures are produced by Rydberg series of narrow resonances converging to the various excitation thresholds. These resonances are related to the trapping of the scattering electron to the highly excited nl states. A set of strong and wide resonances can also be seen in the energy region from 0.3 to 0.4 Ry. The strong interaction between outer electrons can cause these wide resonances, and it most likely corresponds to autoionizing states with excited $3d$ electron.

Similar resonance structures were also found in the R-matrix calculations of Bautista et al. (2009) and Wasson et al. (2010). Visual comparison with their collision strengths in the region below 0.3 Ry shows good qualitative agreement both in regard to the position of resonances and their magnitude. Detailed comparison of such substantial resonance structures is not possible. More important is the overall contribution of resonances to the rate coefficients and the agreement between the background collision strengths. In this respect we should note that our collision strengths also show strong resonance structures at higher electron energies, not detected in the previous calculations due to omission of the higher target thresholds of the $3d^34s4p$ configuration. These states have strong connection with the lower $3d^44s$ and $3d^44p$ states through the strong $3d$–$4p$ or $3d$–$4s$ interactions and thereby should lead to the additional CC effects, and therefore to the additional resonance structures. These resonances may contribute considerably to the collision rate parameters.

The Maxwellian averaged collision strengths for the selected forbidden transitions are presented in Figure 4. The present results have been compared with the other available R-matrix calculations. We denote the 162-state R-matrix calculation of Bautista et al. (2009) by RM-162, the 280-state R-matrix calculation of Wasson et al. (2010) by RM-280, and the present calculation as BSR-512. As seen from the figure, the effective collision strengths obtained in different models differ in both magnitude and the temperature behavior. The upper panels represent the three lowest lying fine structure transitions from the ground state to the first three metastable $3d^5\ ^6S_{1/2} \rightarrow 3d^44s\ ^6D_{3/2,5/2,7/2}$ levels, that is, 1–2, 1–3, and 1–4 transitions. The present effective collision strengths lie consistently higher than the RM-280 results for all three transitions and for all temperatures. Differences are approximately 25% at higher temperatures and reach up to 50% at lower temperatures. A closer agreement is noticed with the RM-162 results of Bautista et al. (2009); however, at lower temperatures the differences are still about 20%. The comparison indicates that the background collision strengths are consistently higher in the present calculations than the RM-280 model. The background collision strengths are directly connected to the target wave functions and the corresponding atomic potentials. The bigger effective collision strengths at lower temperatures in the present calculations can be due to the enhanced resonance structure in the near-threshold region. Another typical reason for the discrepancies at lower temperatures is the difference in the excitation thresholds as is also discussed by Bautista et al. (2015). Both the present and RM-280 calculations used the target excitation energies that are closer to the experimental values, and thus the above reason may not cause differences between the BSR-512 and RM-280 calculations; however, it may be the reason for differences with the RM-162 results at lower temperatures.

Close agreement between different calculations is obtained for the spin changing transitions $3d^5\ ^6S_{5/2} \rightarrow 3d^44s\ ^4D_{1/2,3/2,5/2}$ (1–7, 1–8, and 1–9), presented in the middle panels of Figure 4. In this case, the effective collision strengths agree closely for all temperatures, with some small differences with RM-162 results at lower temperatures which may be attributed to the lower resolution of the resonance structure in the RM-162 model in the near-threshold region. The results for transitions between excited states, namely, the

Table 4

Comparison of Transition Probabilities (10^{-7} s^{-1}) for Selected E1 Lines of Cr II with Measurements of Nilsson et al. (2006; N2006) and Lawler et al. (2017; L2017)

Upper Level	Lower Level	Present	N2006	L2017	Upper Level	Lower Level	Present	N2006	L2017
$3d^4(^5D)4p\ ^6F^o_{1/2}$	$3d^4(^5D)4s\ ^6D_{1/2}$	20.00	17.70	17.60	$3d^4(^5D)4p\ ^4F^o_{7/2}$	$3d^4(^5D)4s\ ^4D_{5/2}$	17.50	16.50	15.60
	$3d^4(^5D)4s\ ^6D_{3/2}$	5.65	5.57	5.67		$3d^4(^5D)4s\ ^4D_{7/2}$	2.37	2.50	2.48
$3d^4(^5D)4p\ ^6F^o_{3/2}$	$3d^4(^5D)4s\ ^6D_{1/2}$	8.04	7.24	7.51		$3d^5\ ^4G_{9/2}$	3.33	3.97	3.92
	$3d^4(^5D)4s\ ^6D_{3/2}$	14.60	13.60	13.60	$3d^4(^5D)4p\ ^4F^o_{9/2}$	$3d^4(^5D)4s\ ^6D_{9/2}$	0.32	0.50	0.28
	$3d^4(^5D)4s\ ^6D_{5/2}$	3.03	2.95	2.73		$3d^4(^5D)4s\ ^4D_{7/2}$	19.70	18.60	18.20
$3d^4(^5D)4p\ ^6F^o_{5/2}$	$3d^4(^5D)4s\ ^6D_{3/2}$	12.40	11.30	11.30		$3d^5\ ^4G_{11/2}$	3.54	4.21	4.30
	$3d^4(^5D)4s\ ^6D_{5/2}$	11.90	11.10	11.10		$3d^5\ ^4D_{7/2}$	0.09	0.21	0.15
	$3d^4(^5D)4s\ ^6D_{7/2}$	1.44	1.44	1.36	$3d^4(^5D)4p\ ^4D^o_{1/2}$	$3d^4(^5D)4s\ ^4D_{1/2}$	10.20	7.73	7.90
$3d^4(^5D)4p\ ^6F^o_{7/2}$	$3d^4(^5D)4s\ ^6D_{5/2}$	16.70	15.20	15.20		$3d^4(^5D)4s\ ^4D_{3/2}$	10.70	8.50	8.20
	$3d^4(^5D)4s\ ^6D_{7/2}$	8.76	8.66	8.68		$3d^5\ ^4D_{1/2}$	1.59	1.88	2.15
	$3d^4(^5D)4s\ ^6D_{9/2}$	0.47	0.48	0.54		$3d^5\ ^4D_{3/2}$	1.70	1.93	2.31
$3d^4(^5D)4p\ ^6F^o_{9/2}$	$3d^4(^5D)4s\ ^6D_{7/2}$	21.30	18.90	19.20		$3d^5\ ^4F_{3/2}$	0.95	1.63	1.39
	$3d^4(^5D)4s\ ^6D_{9/2}$	4.84	4.87	4.64	$3d^4(^5D)4p\ ^4D^o_{3/2}$	$3d^4(^5D)4s\ ^4D_{1/2}$	4.71	3.74	3.76
$3d^4(^5D)4p\ ^6F^o_{11/2}$	$3d^4(^5D)4s\ ^6D_{9/2}$	26.40	25.00	25.00		$3d^4(^5D)4s\ ^4D_{3/2}$	8.30	6.60	6.40
$3d^4(^5D)4p\ ^6D^o_{1/2}$	$3d^4(^5D)4s\ ^6D_{1/2}$	5.00	4.29	4.00		$3d^4(^5D)4s\ ^4D_{5/2}$	7.87	6.37	6.00
	$3d^4(^5D)4s\ ^6D_{3/2}$	17.30	14.50	13.10		$3d^5\ ^4D_{1/2}$	0.87	0.96	1.14
	$3d^4(^5D)4s\ ^4D_{1/2}$	2.35	2.02	2.83		$3d^5\ ^4D_{3/2}$	1.23	1.49	1.65
	$3d^4(^5D)4s\ ^4D_{3/2}$	2.27	2.10	2.76		$3d^5\ ^4D_{5/2}$	1.27	1.53	1.71
$3d^4(^5D)4p\ ^6D^o_{3/2}$	$3d^4(^5D)4s\ ^6D_{1/2}$	6.91	6.24	5.67		$3d^5\ ^4F_{5/2}$	0.51	0.79	1.00
	$3d^4(^5D)4s\ ^6D_{3/2}$	0.71	0.56	0.60	$3d^4(^5D)4p\ ^4D^o_{5/2}$	$3d^4(^5D)4s\ ^4D_{3/2}$	4.26	3.28	3.46
	$3d^4(^5D)4s\ ^6D_{5/2}$	12.90	10.90	9.80		$3d^4(^5D)4s\ ^4D_{5/2}$	12.10	9.55	9.30
	$3d^4(^5D)4s\ ^4D_{1/2}$	0.37	0.30	0.45		$3d^4(^5D)4s\ ^4D_{7/2}$	4.52	3.70	3.33
	$3d^4(^5D)4s\ ^4D_{3/2}$	1.93	1.58	2.29		$3d^5\ ^4P_{5/2}$	0.46	1.24	0.63
	$3d^4(^5D)4s\ ^4D_{5/2}$	3.75	3.17	4.70		$3d^5\ ^4P_{3/2}$	0.32	0.32	0.49
$3d^4(^5D)4p\ ^6D^o_{5/2}$	$3d^4(^5D)4s\ ^6D_{3/2}$	8.42	8.02	6.70		$3d^5\ ^4D_{7/2}$	0.77	0.85	1.03
	$3d^4(^5D)4s\ ^6D_{5/2}$	4.30	4.29	3.73		$3d^5\ ^4D_{3/2}$	0.87	0.97	1.15
	$3d^4(^5D)4s\ ^6D_{7/2}$	6.03	4.39	3.85		$3d^5\ ^4D_{5/2}$	1.85	1.99	2.57
	$3d^4(^5D)4s\ ^4D_{5/2}$	1.31	1.02	1.37		$3d^5\ ^4F_{7/2}$	0.79	0.79	1.19
	$3d^4(^5D)4s\ ^4D_{7/2}$	4.79	3.61	5.10		$3d^5\ ^4F_{5/2}$	0.14	0.20	0.27
	$3d^5\ ^4P_{5/2}$	0.49	0.50	0.64	$3d^4(^5D)4p\ ^4D^o_{7/2}$	$3d^4(^5D)4s\ ^4D_{5/2}$	2.57	2.10	2.08
	$3d^5\ ^4P_{3/2}$	0.19	0.18	0.21		$3d^4(^5D)4s\ ^4D_{7/2}$	18.40	15.40	13.30
$3d^4(^5D)4p\ ^6D^o_{7/2}$	$3d^4(^5D)4s\ ^6D_{5/2}$	9.72	9.19	9.80		$3d^5\ ^4P_{5/2}$	0.48	0.44	0.68
	$3d^4(^5D)4s\ ^6D_{7/2}$	13.10	11.90	10.40		$3d^5\ ^4D_{7/2}$	3.10	3.14	4.70
	$3d^4(^5D)4s\ ^6D_{9/2}$	6.71	5.13	5.97		$3d^5\ ^4D_{5/2}$	0.69	0.67	0.82
$3d^4(^5D)4p\ ^6D^o_{9/2}$	$3d^4(^5D)4s\ ^6D_{7/2}$	5.68	5.28	5.10		$3d^5\ ^4F_{9/2}$	0.94	0.89	
	$3d^4(^5D)4s\ ^6D_{9/2}$	23.70	20.90	20.90	$3d^4(^5D)4p\ ^4P^o_{1/2}$	$3d^4(^5D)4s\ ^6D_{1/2}$	1.56	1.68	1.65
	$3d^4(^5D)4s\ ^4D_{7/2}$	0.14	0.15	0.22		$3d^4(^5D)4s\ ^6D_{3/2}$	5.54	6.13	5.10
$3d^4(^5D)4p\ ^4F^o_{3/2}$	$3d^4(^5D)4s\ ^4D_{1/2}$	14.50	13.60	14.10		$3d^4(^5D)4s\ ^4D_{1/2}$	6.62	5.43	6.18
	$3d^4(^5D)4s\ ^4D_{3/2}$	5.30	5.05	5.04		$3d^4(^5D)4s\ ^4D_{3/2}$	6.32	5.28	5.85
	$3d^5\ ^4G_{5/2}$	3.64	4.35	3.82		$3d^5\ ^4P_{3/2}$	0.95	1.13	0.98
$3d^4(^5D)4p\ ^4F^o_{5/2}$	$3d^4(^5D)4s\ ^4D_{3/2}$	15.50	14.60	14.30	$3d^4(^5D)4p\ ^4P^o_{3/2}$	$3d^4(^5D)4s\ ^6D_{1/2}$	5.38	6.24	5.20
	$3d^4(^5D)4s\ ^4D_{5/2}$	4.37	4.36	4.06		$3d^4(^5D)4s\ ^6D_{3/2}$	0.62	0.93	0.78
	$3d^5\ ^4G_{7/2}$	3.29	4.19	3.60		$3d^4(^5D)4s\ ^4D_{3/2}$	3.80	3.12	3.60

fine structure transitions from the $3d^44s\ ^6D_{1/2}$ level to the higher lying $3d^44s\ ^4D_{1/2,3/2,5/2}$ levels (2–7, 2–8 and 2–9 transitions), are given in the lower panels of Figure 4. In this case the different calculations predict rather different effective collision strengths. The RM-162 results are considerably lower than other two calculations at all temperatures. The effective collision strengths from the BSR-512 and RM-280 models approach each other at higher temperatures. This is due to the similar nonresonant collision strengths in the BSR-512 and RM-280 models. However, at lower temperatures there are big discrepancies, indicating significantly different resonance structure in the near-threshold region. It appears that the resonance structure in the near-threshold region is not generated accurately in the RM-280 calculation.

There are significant discrepancies between the available calculations for the effective collision strengths of forbidden transitions in Cr II. While for some transitions agreement is excellent, for others the present BSR-512 calculations predict higher effective collision strengths, especially at lower temperatures. For a few transitions, the converse is true. To

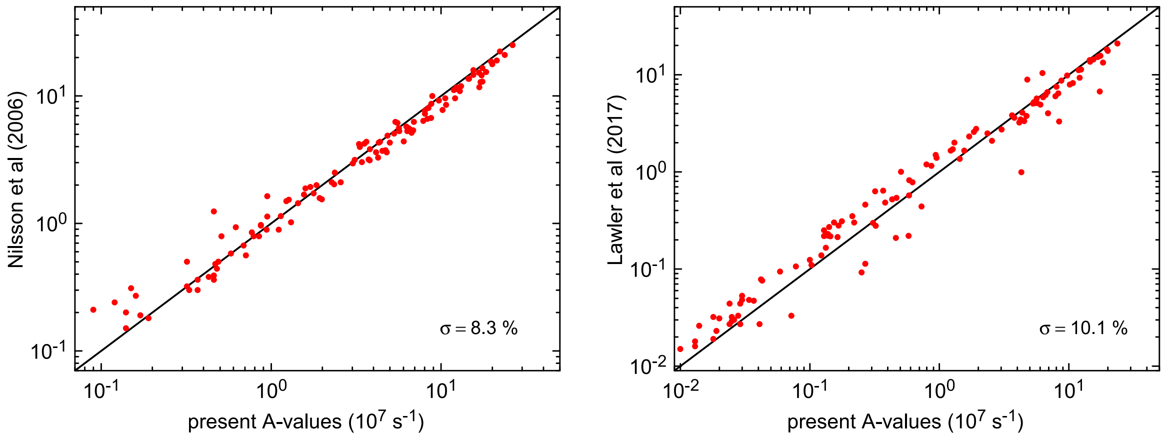

Figure 2. Comparison of the present radiative rates with experimental values of Nilsson et al. (2006) and Lawler et al. (2017).

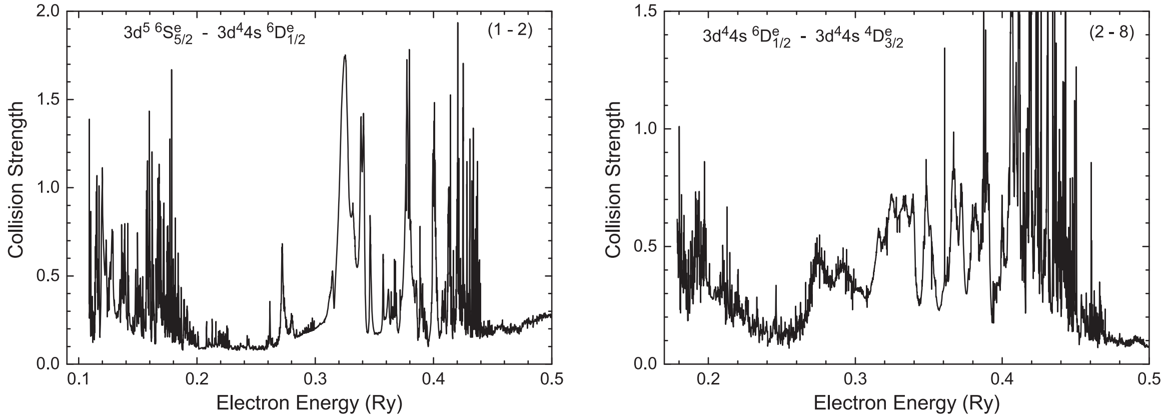

Figure 3. Collision strengths as a function of incident electron energy (in Ry) for the fine structure $3d^5\ ^6S_{1/2}$–$3d^44s\ ^6D_{1/2}$ (1–2) and $3d^44s\ ^6D_{1/2}$–$3d^44s\ ^4D_{3/2}$ (2–8) transitions.

obtain a more systematic estimation, we have compared the present BSR-512 results with the effective collision strengths from the RM-280 model at three different temperatures in Figure 5. The comparison is presented for all forbidden transitions among the lowest 28 even-parity states reported by Wasson et al. (2010). The worst agreement between the two calculations is seen at lower temperatures where the average deviation is approximately 22%. However, there are substantial differences between the two calculations for some individual transitions. The near-threshold resonance structures contribute substantially to the effective collision strengths at lower temperatures and may depend upon the target excitation thresholds and the size of CC expansions. The present resonance structure is expected to be more accurate due to the use of accurate excitation thresholds and extensive CC expansion.

It is clear from the Figure 5 that the agreement gets better for the intermediate temperatures around $T = 10^4$ K with average deviation of about 18%. There is an improvement in agreement with increasing temperatures except for a few transitions. There is generally good agreement in nonresonant collision strengths and the differences appear to be caused by the discrepancies in resonance structures. However, there are a few transitions with weaker physical resonance structures and probable presence of pseudo-resonance structure at higher electron energies may cause the differences. Wang et al. (2017) discussed the influence of the strong pseudo-resonance structures that can change the collision strengths. Comparison of results in Figure 5 can provide an overall accuracy estimate for the available effective collision strengths.

The effective collision strengths for the optically allowed transitions from the $3d^5$ and $3d^44s$ even-parity configuration levels to the $3d^44p$ odd parity configuration levels are given in Figure 6. Comparison is made with the RM-280 calculations of Wasson et al. (2011) and the RM-162 work of Bautista et al. (2009). Here we consider the same transitions that were discussed by Wasson et al. (2011). We first discuss transitions from the ground $3d^5\ ^6S_{5/2}$ state of Cr II to the lowest odd parity $3d^44p\ ^6P_J$ multiplet with fine-structure levels $J = 3/2, 5/2, 7/2$ (1–83, 1–84, and 1–85 transitions), and these are presented in the top panels of Figure 6. For low temperatures, close agreement between all calculations is evidently seen for all three transitions. The resonance structure in the threshold energy region is generally very weak for these transitions and provides only limited contribution to the effective collision strengths. At higher temperatures small deviations occur, with the RM-280 result being higher than other results. Note that the highest temperature considered by Bautista et al. (2009) is $T = 30{,}000$ K.

The transitions from the metastable level $3d^44s\ ^6D_{7/2}$ to the $3d^44p\ ^6D_J$ for $J = 5/2, 7/2$, and $9/2$ levels (5–88, 5–91, 5–93 transitions) are presented in the middle panels of Figure 6. Our effective collision strengths exhibit good agreement with the RM-280 results for the $3d^44s\ ^6D_{7/2} \rightarrow 3d^44p\ ^6D_{7/2,9/2}$ transitions for all temperatures, but the RM-280 and RM-162 results lie significantly higher than the present values for the $3d^44s\ ^6D_{7/2} \rightarrow 3d^44p\ ^6D_{5/2}$ transition at all temperatures.

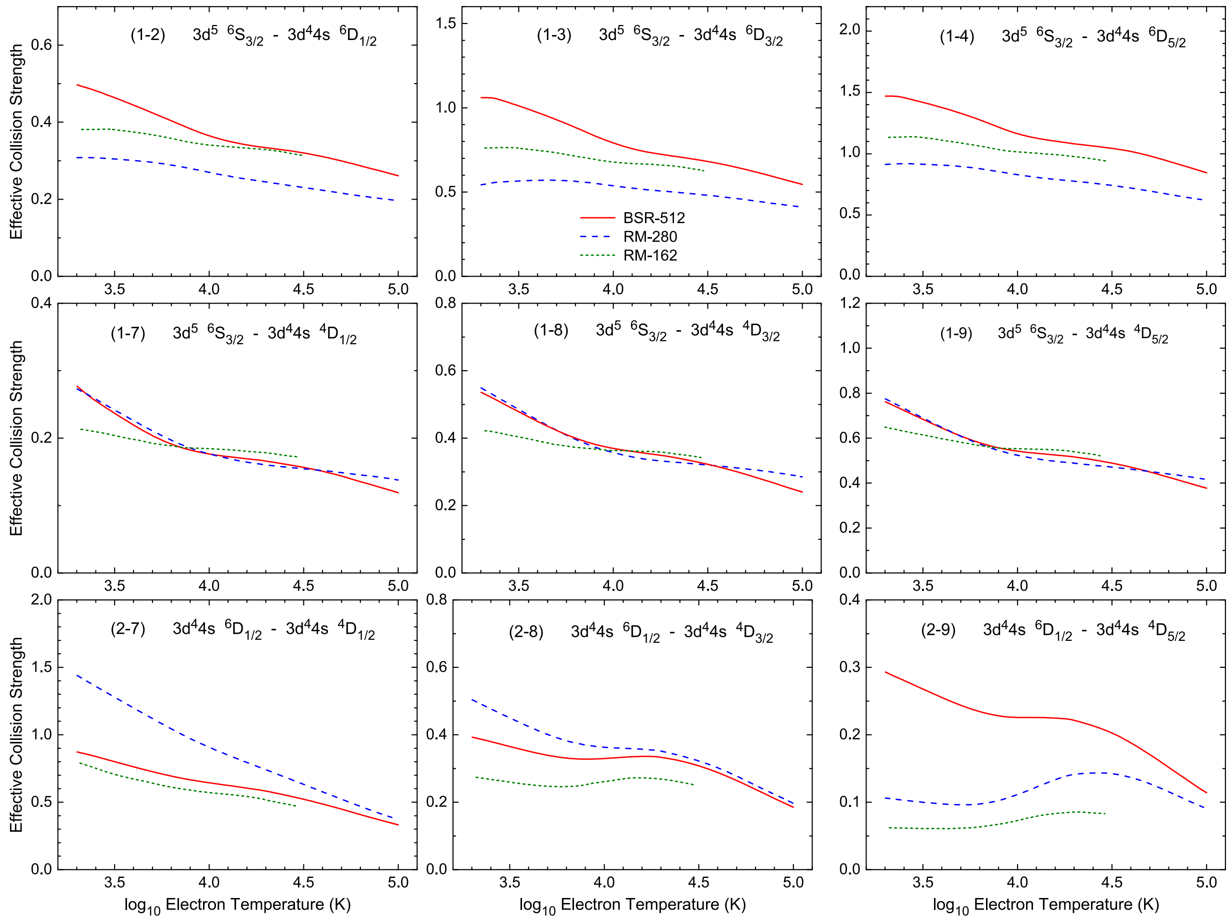

Figure 4. Effective collision strengths as a function of electron temperature (in K) on log scale for selected dipole-forbidden transitions in Cr II. The solid (red) line represents the present work, the dashed (blue) line represents the RM-280 calculation of Wasson et al. (2011), and the dotted–dashed (green) line is the work of Bautista et al. (2009).

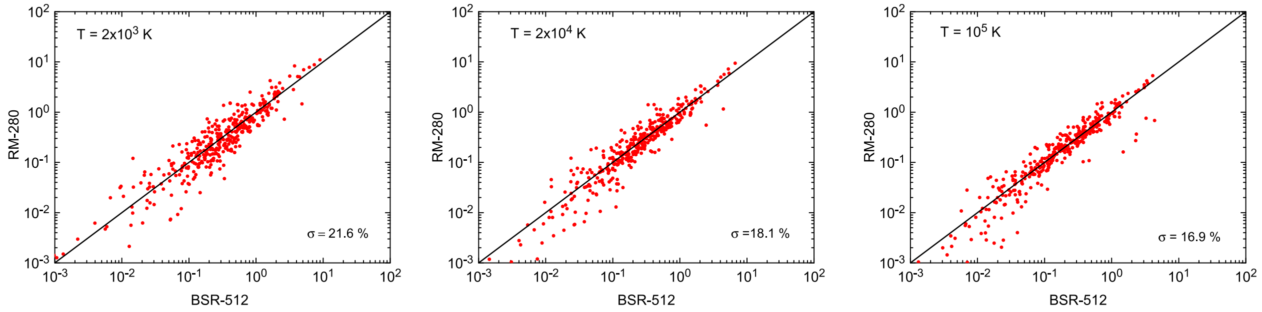

Figure 5. Comparison of effective collision strengths from the present BSR-512 model with the RM-280 calculations of Wasson et al. (2010) at three temperatures 2×10^3, 2×10^4, and 10^5 K. The comparison is made for all transitions between the first 28 Cr II levels. The average deviation of the BSR-512 results with Wasson et al. (2010) is also shown at each temperature.

The discrepancies can be caused by an insufficient number of partial waves. The higher partial waves with large total orbital angular momenta make the dominant contribution to the dipole-allowed transitions at higher electron energies. Wasson et al. (2011) devoted a large part of their discussion to this problem, comparing the results with and without the top-up procedure. Direct calculations in their RM-280 model were carried out for $2J = 26$ followed by a top-up procedure using the Coulomb–Bethe approximation. The present BSR calculations include all partial waves up to $2J = 48$ with higher partial wave contributions included via a similar top-up procedure. We believe that both calculations included contribution from higher partial waves to full extent and higher partial waves cannot be a reason for observed discrepancies. In contrast, as seen from Figure 6, the results from Bautista et al. (2009) clearly underestimate the effective collision strengths at higher temperatures, indicating a problem with higher partial wave contributions in their calculations.

The discrepancies between the present and RM-280 collision strengths for the electric-dipole transitions are likely produced by the differences in oscillator strengths. The collision strengths for dipole-allowed transitions at high energies depend on the oscillator strengths. The oscillator strengths for transitions presented in Figure 6 are listed in Table 5. The effective collision strengths for these dipole-allowed transitions show agreement or disagreement similar to their oscillator strengths. For example, our

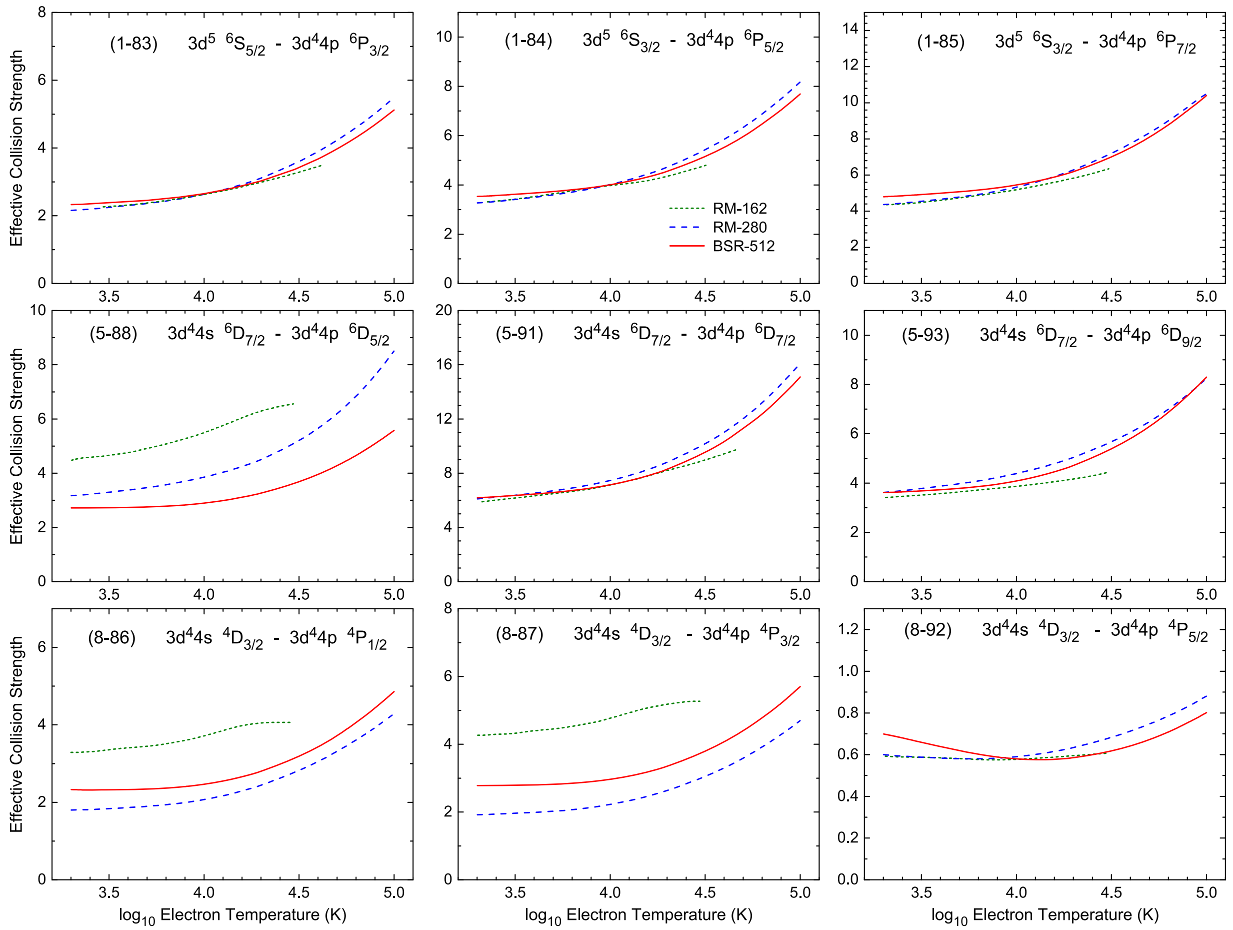

Figure 6. Effective collision strengths as a function of electron temperature (in K) on log scale for selected dipole-allowed transitions in Cr II. The solid (red) line denotes the present work, the dashed (blue) line corresponds to RM-280 calculations of Wasson et al. (2011), the dotted–dashed (green) line is the work of Bautista et al. (2009).

Table 5
Weighted Oscillator Strengths (gf_{ij}) Values for Transitions in Cr II Considered in the Figure 6

i	*j*	Present Work	Wasson et al. (2011)	Nilsson et al. (2006)
1	83	0.289	0.481	0.300
	84	0.654	0.719	0.487
	85	1.018	0.958	0.651
5	88	0.296	0.642	0.287
	91	1.120	1.075	1.025
	93	0.755	0.569	0.561
8	86	0.212	0.166	0.186
	87	0.264	0.212	0.216
	92	0.050	0.034	0.029

oscillator strength for the $3d^44s\ ^6D_{7/2} \rightarrow 3d^44p\ ^6D_{5/2}$ (5–88) transition is in close agreement with the experimental value of Nilsson et al. (2006), but two times smaller than the value of Wasson et al. (2011). A similar difference can be seen for the corresponding effective collision strengths. Our target wave function expansions show that the $3d^44p\ ^6D_{7/2}$ and $^6D_{9/2}$ states exhibit very small term mixing, whereas the $^6D_{5/2}$ level mixes very strongly with the $^4D_{5/2}$ term with almost 50% mixing coefficient. The term mixing crucially depends on the details of the calculations such as accurate representation of the position of corresponding LS terms. We believe that our expansions represent the term mixing most accurately, due to the fine-turning procedure for the LS terms described above. It is also confirmed by close agreement with the experimental oscillator strengths. Summarizing, the $3d^44s\ ^6D_{7/2} \rightarrow 3d^44p\ ^6D_{5/2}$ (5–88) transition is a typical example illustrating the importance of term mixing for the accurate calculation of collision strengths.

We found a similar behavior for the $3d^44s\ ^4D_{3/2} \rightarrow 3d^44p\ ^4P_{1/2,3/2,5/2}$ (8–86, 8–87, and 8–92) transitions presented in the bottom panels of Figure 6. The RM-162 collision strengths are larger than the present results for the 8–86 and 8–87 transitions; however, close agreement is observed for the 8–92 transition. The agreement of our results with the RM-280 effective collision strength is much better for all transitions. This again would suggest that there is considerable term mixing for these fine-structure levels. As seen from Table 5, our oscillator strengths and the results of Wasson et al. (2011) are both in close agreement with the experimental values of Nilsson et al. (2006). The 10%–20% difference in the corresponding effective collision strengths from the two calculations might have been caused by different target expansions.

The present effective collision strengths for the electric-dipole-allowed transitions have been compared with the RM-280 model in Figure 7 at three temperatures. The present results exhibit considerable differences with the RM-280 model. The average deviation between the two models is around 30%. If we consider only the transitions from the ground state, the agreement will be on the same level. For some weak as well as

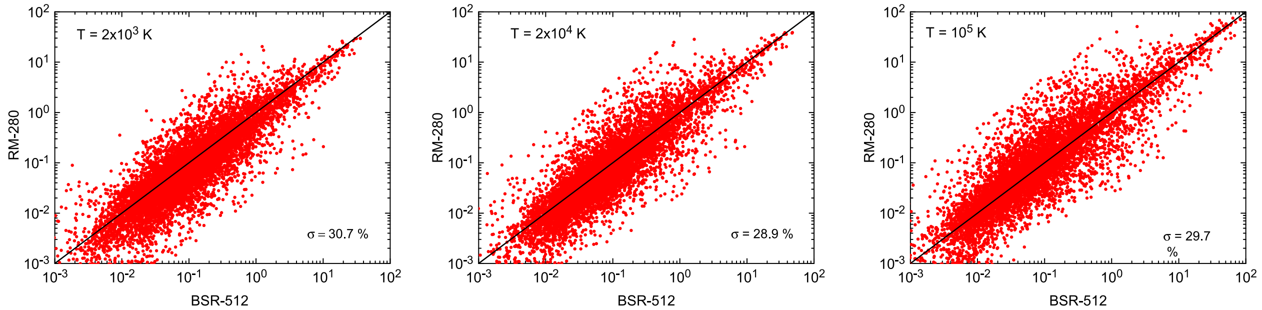

Figure 7. Comparison of effective collision strengths from the BSR-512 model with the RM-280 calculations of Wasson et al. (2011) at three temperatures. The comparison is made for all dipole-allowed transitions between 280 levels of Cr II in the RM-280 model. Also indicated in each panel is the average deviation of the latter from the BSR-512 results.

Table 6

Electron Excitation Effective Collision Strengths for Fine-structure Transitions in Cr II

i	j	1000 K	1500 K	2000 K	2300 K	2500 K	5000 K	7500 K	10,000 K	13,000 K	15,000 K
1	2	5.34E–01	5.13E–01	4.97E–01	4.88E–01	4.83E–01	4.26E–01	3.87E–01	3.64E–01	3.49E–01	3.43E–01
1	3	1.03E+00	1.06E+00	1.06E+00	1.06E+00	1.05E+00	9.35E–01	8.44E–01	7.89E–01	7.53E–01	7.39E–01
1	4	1.41E+00	1.46E+00	1.47E+00	1.47E+00	1.46E+00	1.34E+00	1.23E+00	1.16E+00	1.12E+00	1.11E+00
1	5	1.87E+00	1.99E+00	2.02E+00	2.02E+00	2.01E+00	1.83E+00	1.66E+00	1.57E+00	1.51E+00	1.49E+00
1	6	1.66E+00	1.72E+00	1.73E+00	1.73E+00	1.73E+00	1.64E+00	1.54E+00	1.50E+00	1.49E+00	1.50E+00
1	6	1.66E+00	1.72E+00	1.73E+00	1.73E+00	1.73E+00	1.64E+00	1.54E+00	1.50E+00	1.49E+00	1.50E+00

(This table is available in its entirety in machine-readable form.)

strong transitions, the results differ from each other by several orders of magnitude. Perhaps the different target representations and term mixing caused large differences. Table 6 shows the effective collision strengths $\Upsilon_{i-j}(T_e)$ over a broad range of 20 temperatures from 1000 to 100,000 K. The effective collision strengths are listed for transitions between the 512 fine-structure levels and cover emission lines in various wavelength regions including infrared, optical, and ultraviolet lines. The results should be useful for modeling and diagnostics of stellar and nebular astrophysical plasmas. The i and j indicate the indices of lower and upper levels, respectively, as given in the Table 1. The entire contents of the Table 6 have been published online in a machine-readable format with an associated ReadMe file.

4. Summary

In the present work, we have computed effective collision strengths and radiative parameters for all forbidden and optically allowed transitions between the 512 fine-structure levels of Cr II $3d^44s$, $3d^5$, $3d^44p$, $3d^34s^2$, and $3d^34s4p$ configurations. Inclusion of the additional $3d^34s^2$ and $3d^34s4p$ configurations, which were not considered in previous calculations, leads to a substantial 3492 coupled channels problem. This allowed us to explore the influence of strong $3d$–$4p$ and $3d$–$4s$ excitations on our results. The scattering calculations were carried out using the BSR computer codes. The continuum wave functions have been represented by the B-splines basis. The complicated iron-peak atomic systems required significant modification of the BSR scattering codes. We used nonorthogonal orbitals both for the construction of the target wave functions and for the representation of scattering functions. Accurate description of target states was obtained by optimization of term-dependent atomic wave functions independently and by using extensive CI expansions with carefully chosen configurations. The target level energies were further improved by using a fine-tuning procedure to match experimental values. This process also enhanced the accuracy of the term mixing coefficients in the wave functions that may significantly improve the accuracy of collision strengths.

We have made systematic comparisons with other available calculations to assess the accuracy of our atomic rates. The radiative parameters for optically allowed transitions are in good agreement with the recent measurements by Nilsson et al. (2006) and Lawler et al. (2017). The overall agreement of the present BSR results with previous R-matrix calculations of Wasson et al. (2010, 2011) is very reasonable considering the complexity of the atomic system. Some discrepancies can be explained on the basis of better accuracy of our target wave functions. Comparison between the independent calculations carried out with different computational codes together with different target wave functions and size of CC expansions allowed us to make assessment of the accuracy of the effective collision strengths in these data sets. The closest agreement was noted for the forbidden transitions between lowest even-parity states of Cr II. We would expect that the effective collision strengths for these important low-lying forbidden lines are accurate to within 20%. The same level of accuracy is expected for the strong dipole-allowed transitions. Overall, our results are estimated to be accurate to 30% or better for many of the transitions, with lower accuracy for transitions between closely lying excited levels and to very highly excited levels. Due to the large number of states included in the present calculations, there should be a redistribution of electron flux into the available channels. The accurate wave functions and f-values/A-values used in our CC work illustrate that our effective collision strengths should be used in preference to those in the literature.

The research work was supported by the United States National Science Foundation under grants No. AST-1714159 and No. PHY-0555226. The numerical calculations were performed on STAMPEDE at the Texas Advanced Computing Center. They were made possible by the XSEDE allocations PHY-170047 and PHY-090031.

ORCID iDs

S. S. Tayal https://orcid.org/0000-0003-1805-0930

References

Babel, J., & Lanz, T. 1992, A&A, 263, 232

Backstrom, E., Gurell, J., Royen, P., et al. 2012, MNRAS, 420, 1636

Ballance, C. P., & Griffin, D. C. 2004, JPhB, 37, 2943

Barklem, C., Chrislib, N., Beers, T. C., et al. 2005, A&A, 439, 129

Bautista, M. A., Ballance, C. P., Gull, T. P., et al. 2009, MNRAS, 393, 1503

Bautista, M. A., Fivet, V., Ballance, C. P., et al. 2015, ApJ, 808, 174

Bouazza, S., Quinet, P., & Palmeri, P. 2019, At. Data Nucl. Data Tables, 120, 323

Burgess, A. 1974, JPhB, 7, L364

Burke, P. G., Burke, V. M., & Dunseath, K. M. 1994, JPhB, 27, 5341

Dimitrijevic, M. S., Ryabchikova, T., Simic, Z., et al. 2007, A&A, 469, 681

Froese Fischer, C., Tachiev, G., Gaigalas, G., & Godefroid, M. R. 2007, CoPhC, 176, 559

Gurell, J., Nilsson, L., Engstrom, L., et al. 2010, A&A, 511, A68

Hibbert, A. 1975, CoPhC, 9, 141

Hibbert, A. 1996, PhST, T65, 104

Kramida, K., Ralchenko, Yu., Reader, J. & NIST ASD Team 2015, NIST Atomic Spectra Database (ver. 5.3) (Gaithersburg, MD: National Institute of Standards and Technology), http://physics.nist.gov/asd

Kurucz, R. L. 1988, in Trans. IAU, XXB, ed. M. McNally (Dordrecht: Kluwer), 168

Lawler, J. E., Sneden, C., Nave, G., et al. 2017, ApJS, 28, 10

Lopez-Garcia, Z., Adelman, S. J., & Pintado, O. I. 2001, A&A, 367, 859

Nilsson, H., Ljung, G., Lundberg, H., & Nielsen, K. E. 2006, A&A, 445, 1165

Raassen, A. J. J., & Uylings, P. H. M. 1998, JPhB, 31, 3137

Rice, J. B., & Wehlau, W. H. 1994, A&A, 291, 825

Schade, W., Mundt, B., & Helbig, V. 1990, PhRvA, 42, 1454

Sneden, C., Cowan, J. J., Lawler, J. E., et al. 2003, ApJ, 591, 936

Tayal, S. S., & Zatsarinny, O. 2018, PhRvA, 98, 012706

Wallace, L., & Hinkle, K. 2009, ApJ, 700, 720

Wang, K., Fernandez-Menchero, L., Zatsarinny, O., & Bartschat, K. 2017, PhRvA, 95, 042709

Wasson, I. R., Ramsbottom, C. A., & Norrington, P. H. 2010, A&A, 524, A35

Wasson, I. R., Ramsbottom, C. A., & Scott, M. P. 2011, ApJS, 196, 24

Zatsarinny, O. 2006, CoPhC, 174, 273

Zatsarinny, O., & Froese Fisher, C. 2000, CoPhC, 12, 247

Zatsarinny, O., & Froese Fisher, C. 2009, CoPhC, 180, 2041